Solid-liquid interface charge transfer for generation of H_2O_2 and energy

Yunhao Hu[1, 2], Weifeng Yang[1], Yuji Ma[1], Yong Qiu[3], Wei Wei[1], Bo Wu[1], Kerui Li[1], Yaogang Li[1], Qinghong Zhang[1], Ru Xiao[1], Chengyi Hou[1]* & Hongzhi Wang[1, 2]*

[1] State Key Laboratory for Modification of Chemical Fibers and Polymer Materials, College of Materials Science and Engineering, Donghua University, Shanghai 201620, PR China.
[2] School of Materials Science and Engineering, Shanghai Dianji University, Shanghai 201306, China.
[3] Binjiang Institute of Zhejiang University, Hangzhou, 310053, China.

*Corresponding author: Chengyi Hou (hcy@dhu.edu.cn), Hongzhi Wang (wanghz@dhu.edu.cn)

This PDF file includes:
Figures S1 to S41
Tables S1 to S2

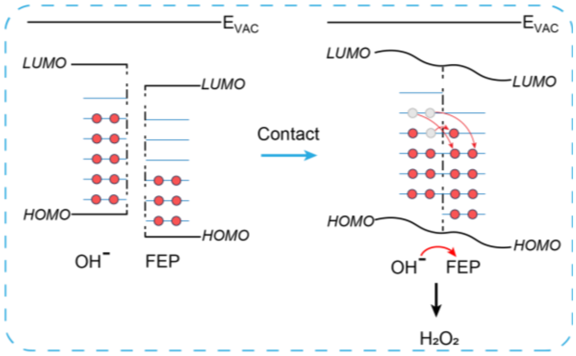

Figure S1 Surface state model for explaining charge interfacial transfer. EVAC: vacuum degree; LUMO: the lowest unoccupied molecular orbital; HOMO: the highest occupied molecular orbital.

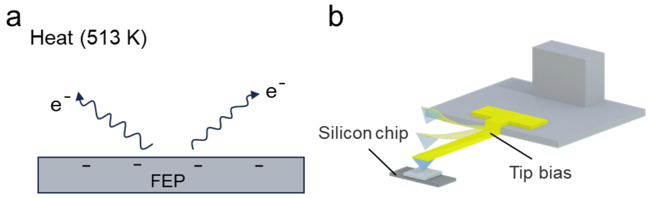

Figure S2 KPFM test of solid surface potential a Thermal emission of electrons on solid surface. **b** Schematic of the apparatus for KPFM measurement of solid surface potential.

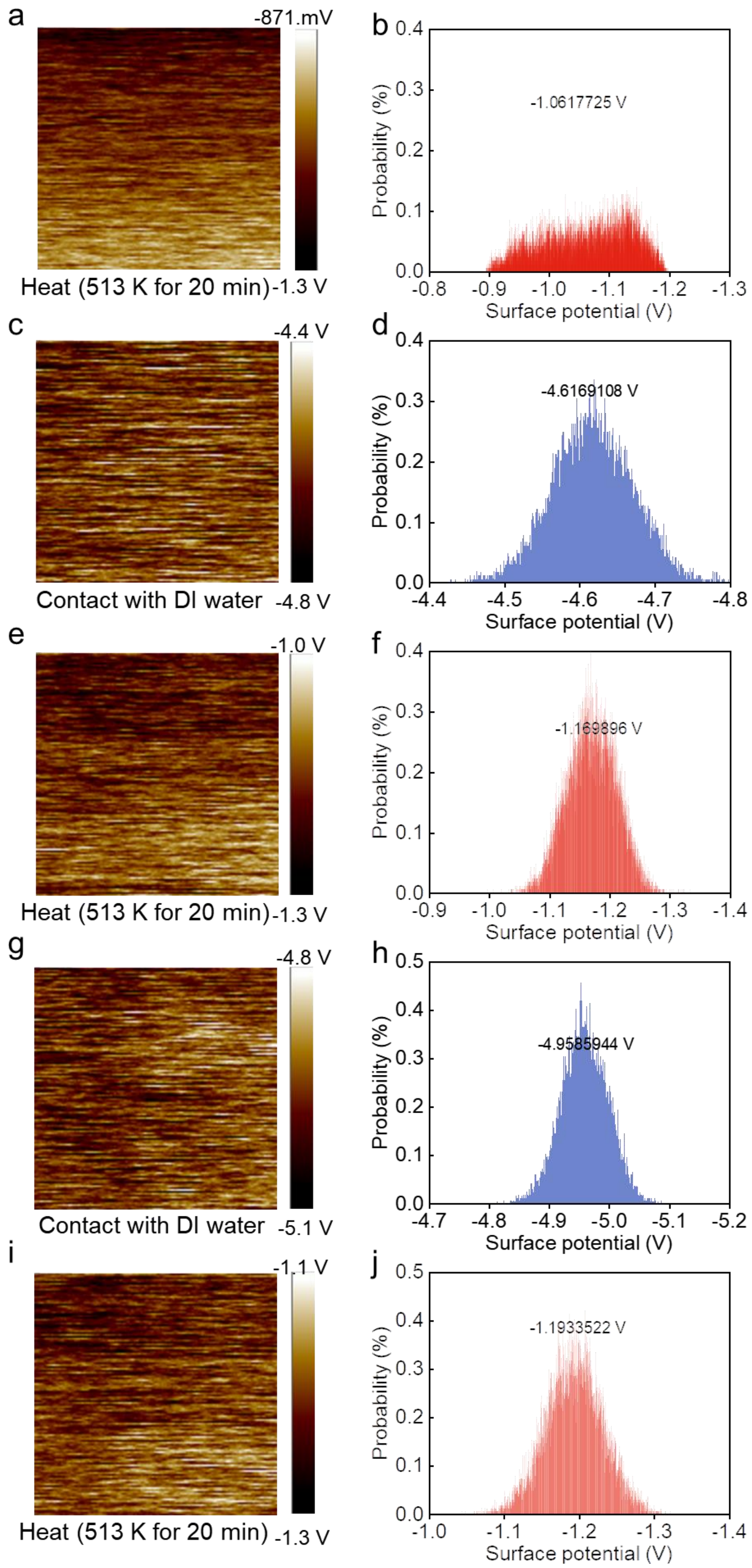

Figure S3 Friction-thermal excitation cycle surface potential test. a, c, e, g, i Solid KPFM images. **b, d, f, h, j** Surface potential distribution of KPFM results.

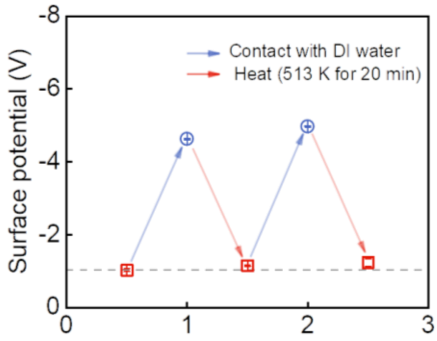

Figure S4 KPFM potential change diagram before and after solid-liquid friction. n = 3 independent samples for each group, data represent mean ± standard deviation.

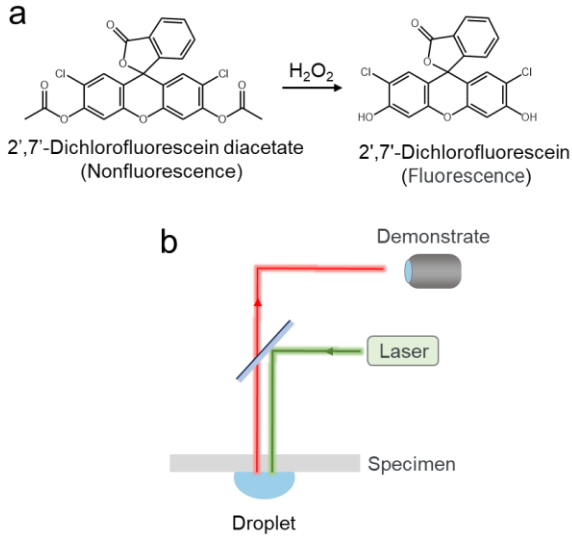

Figure S5 Fluorescence imaging of hydrogen peroxide in water. a Reaction scheme between fluorescent indicator 2',7'-Dichlorofluorescein diacetate and H_2O_2. **b** Schematic diagram of laser scanning confocal microscope.

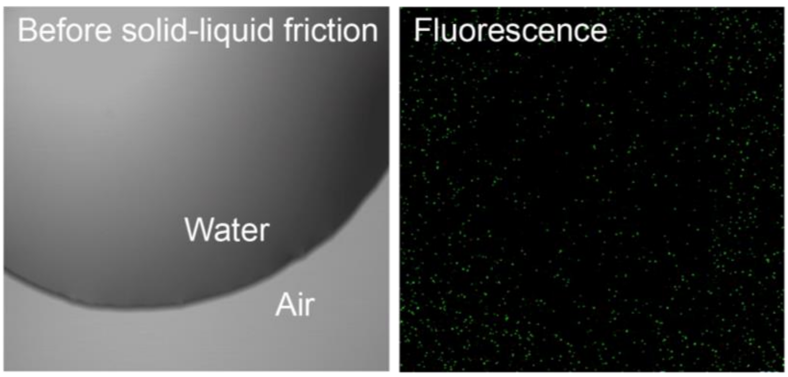

Figure S6 Brightfield and fluorescence images of a mixture of deionized water and DCF-DA.

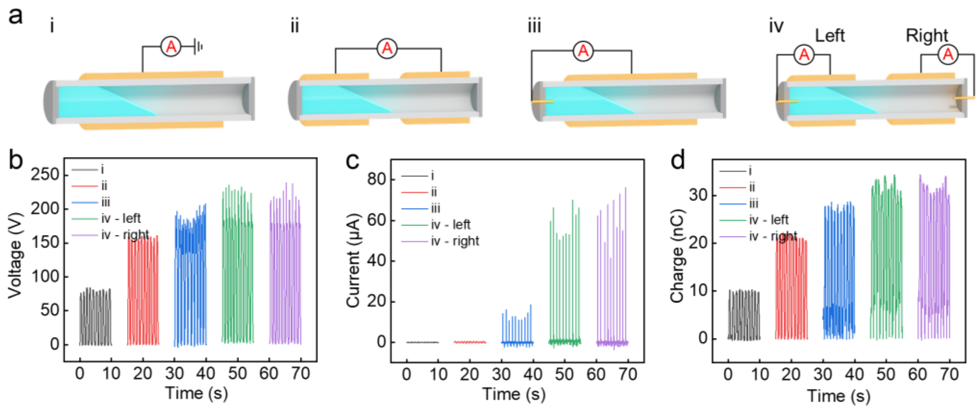

Figure S7 Effects of various electrode structure designs on solid-liquid power generation performance. a Design diagram of different electrode structures. **b** voltage performance output. **c** Current performance output. **d** Charge performance output.

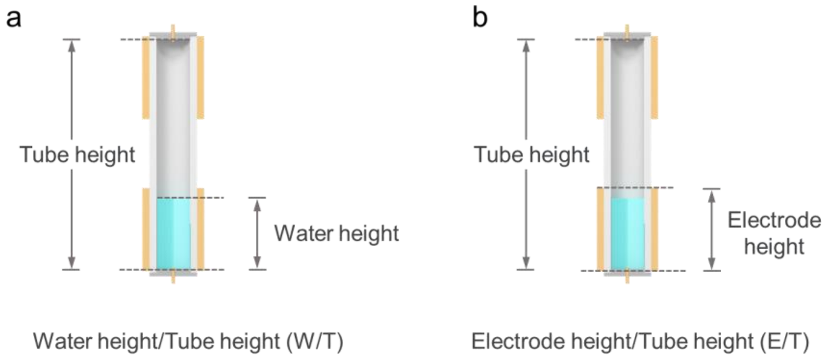

Figure S8 Parameters affecting solid-liquid electrical performance. a Volume occupied by water. **b** External electrode length

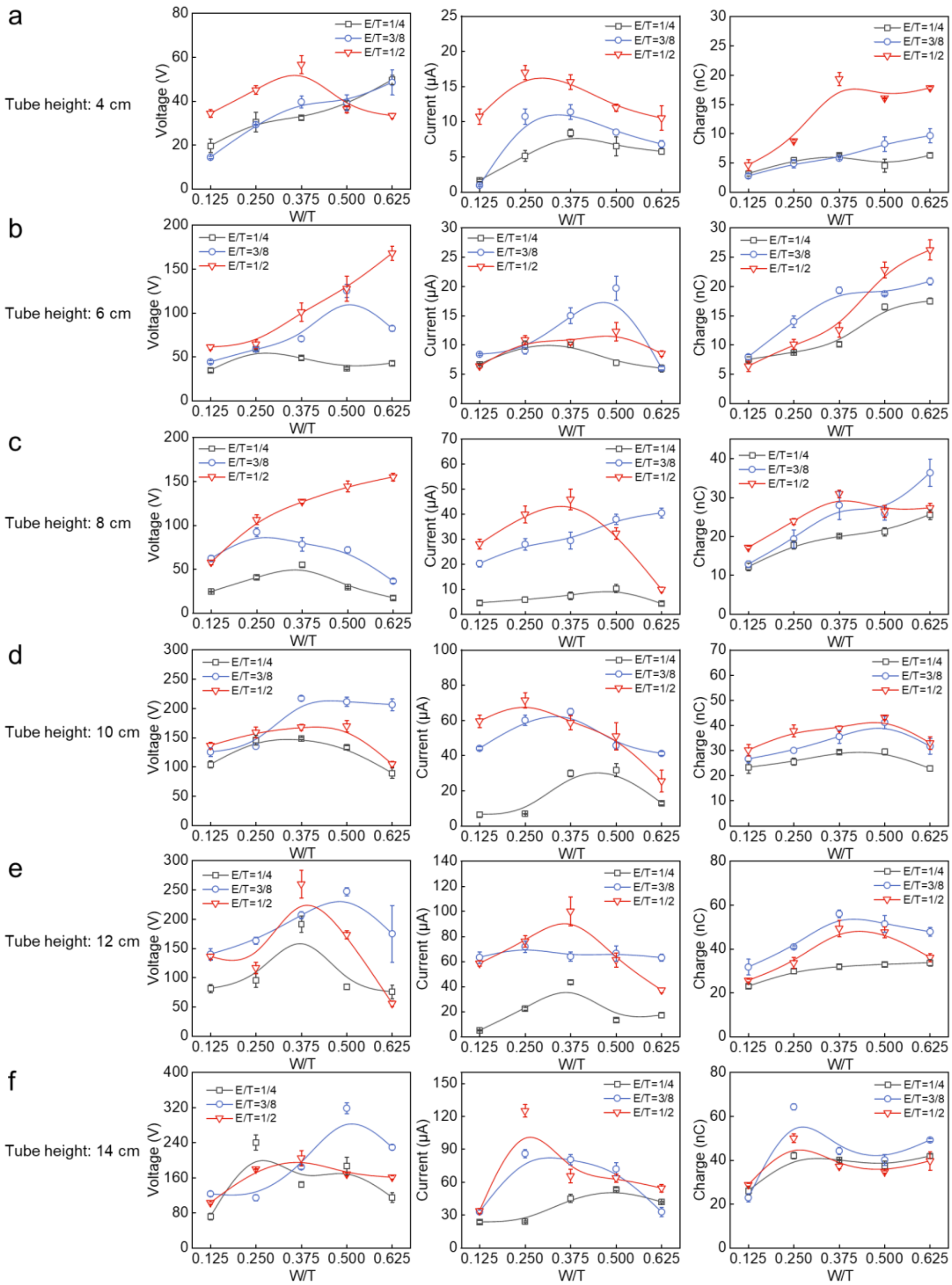

Figure S9 Output of solid-liquid power generation performance under different parameters. Impact of water-to-tube height ratio and electrode-to-tube height ratio on electrical performance output for different tube heights. The heights of the tubes are: **a** 4 cm. **b** 6 cm. **c** 8 cm. **d** 10 cm. **e** 12 cm. **f** 14 cm. n = 3 independent samples for each group, data represent mean ± standard deviation.

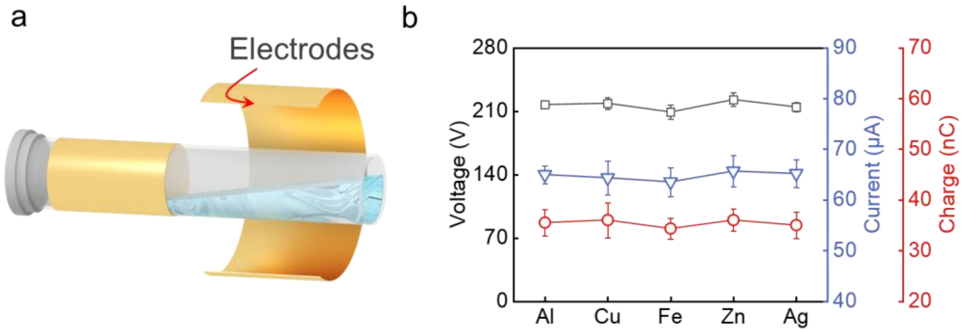

Figure S10 Effect of external electrode types on solid-liquid electrical performance output. a External electrode. **b** Electrical performance output with different external electrode of the device: Al, Cu, Fe, Zn, Ag. n = 3 independent samples for each group, data represent mean ± standard deviation.

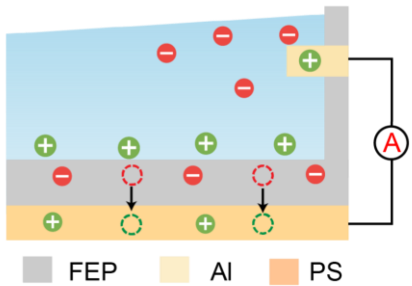

Figure S11 Interface charge recombination.

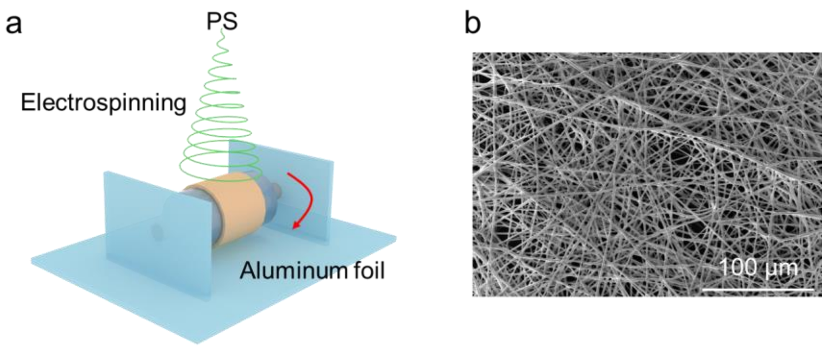

Figure S12 Preparation of PS nanofiber membranes via electrospinning. a Preparation and collection of PS nanofiber membranes. **b** Surface SEM morphology of PS nanofiber membrane

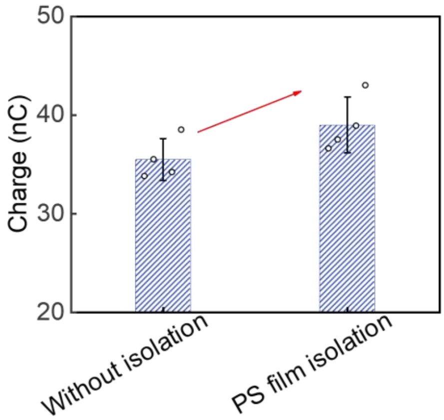

Figure S13 PS isolation structure enhances charge output. n = 4 independent samples for each group, data represent mean ± standard deviation.

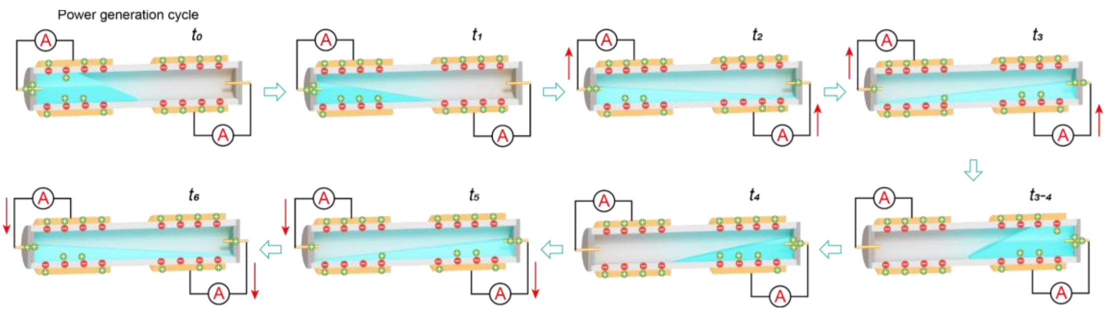

Figure S14 A cycle of charge transfer process. The generator mechanism includes characteristic time points denoted as t_0, t_1, t_2, t_3, t_4, t_5, and t_6. t_0: Water flows to the far left side of the tube. t_1: Water flows just above the Al electrode at the right end. t_2: Water flow detaches from the Ag electrode at the left end. t_3: Water flow contacts the Ag electrode at the right end. t_4: Water flow detaches from just above the Al electrode at the left end. t_5: Water flow detaches from the right Ag electrode. t_s: Water flow contacts the left Ag electrode.

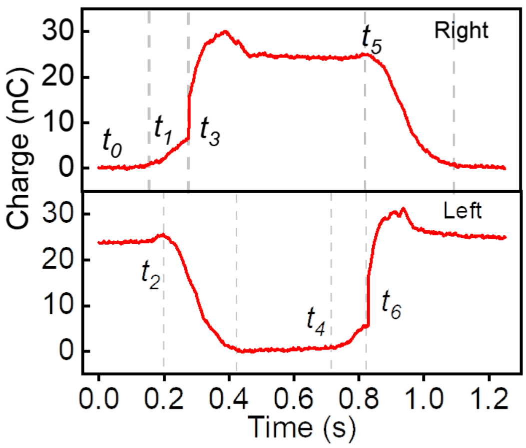

Figure S15 The periodically varying charge transfer signals on the left and right sides.

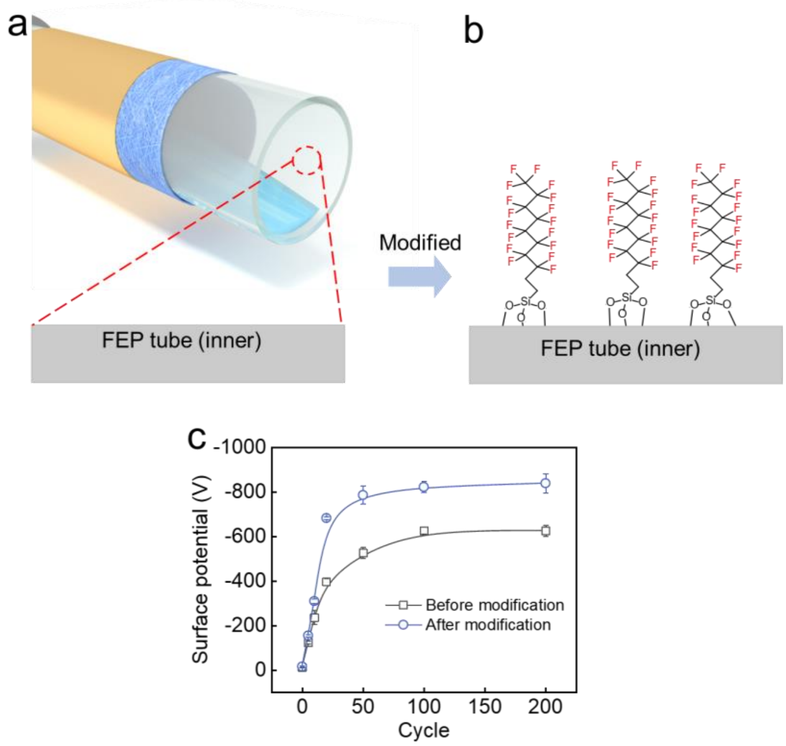

Figure S16 Modification of tube inner wall. a Inner wall of tube. **b** Utilizing DCFH-DA for inner wall tube modification. c Solid surface potential test. n = 3 independent samples for each group, data represent mean ± standard deviation.

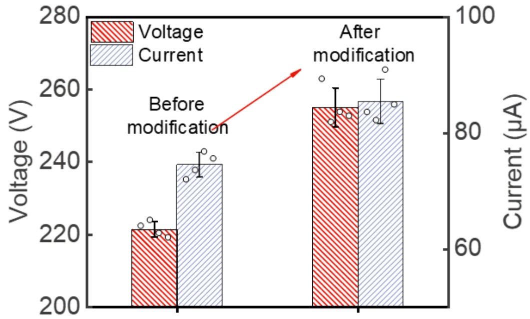

Figure S17 Alterations in Voltage and Current Characteristics Before and After Modification. n = 4 independent samples for each group, data represent mean ± standard deviation.

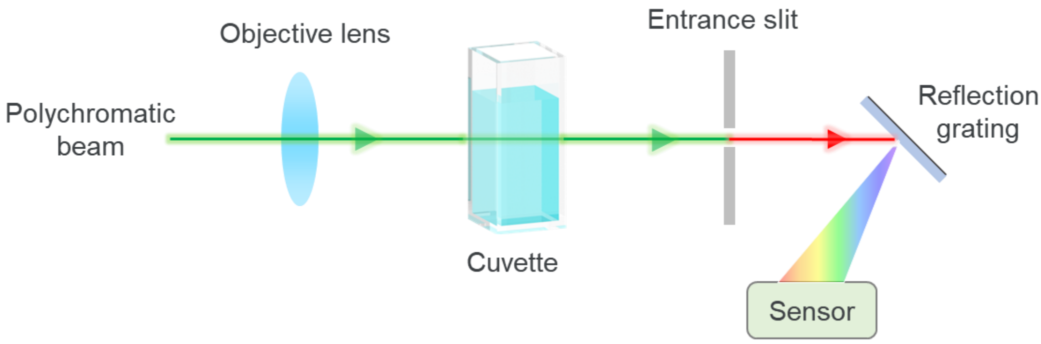

$$2K_2TiO(C_2O_4)_2{\cdot}2H_2O + 3H_2O_2 \rightarrow 2TiO_2 + 2(COOH)_2 + 6H_2O + 2K^+$$

Figure S18 Utilize an UV-Vis-NIR spectrometer to characterize changes in H_2O_2 content.

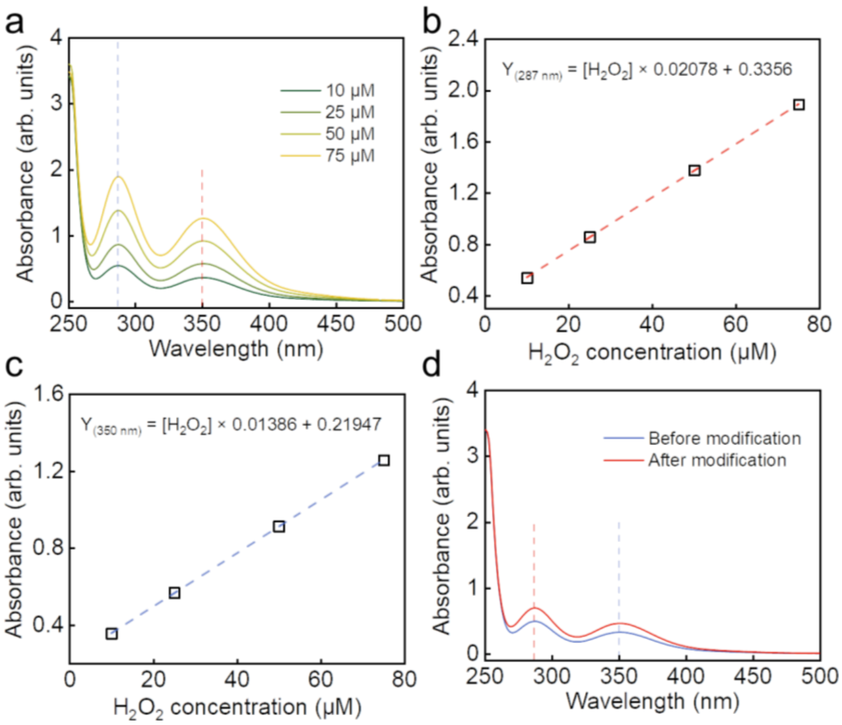

Figure S19 KI method for quantification of H_2O_2. a UV spectrum of H_2O_2 aqueous solution titrated with KI, with H_2O_2 concentrations of 10 μM, 25 μM, 50 μM, and 75 μM. **b** Calibration curve of absorption at 287 nm acquired from the UV absorption spectrum. **c** Calibration curve of absorption at 350 nm acquired from the UV absorption spectrum. **d** UV spectra of water titrated with KI after solid-liquid friction cycles (before and after modification of the inner wall of the tube).

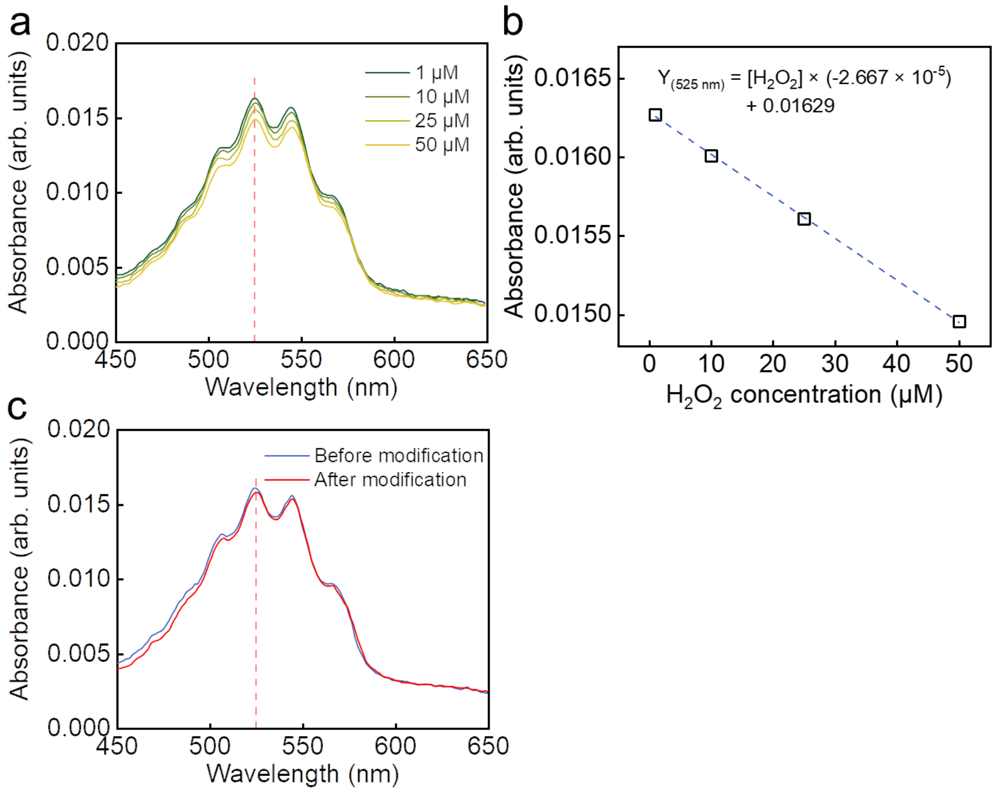

Figure S20 Potassium permanganate method for quantification of H_2O_2. a UV spectrum of H_2O_2 aqueous solution titrated with potassium permanganate, with H_2O_2 concentrations of 1 μM, 10 μM, 25 μM, and 50 μM. **b** Calibration curve of absorption at 525 nm acquired from the UV absorption spectrum. **c** UV spectra of water titrated with potassium permanganate after solid-liquid friction cycles (before and after modification of the inner wall of the tube).

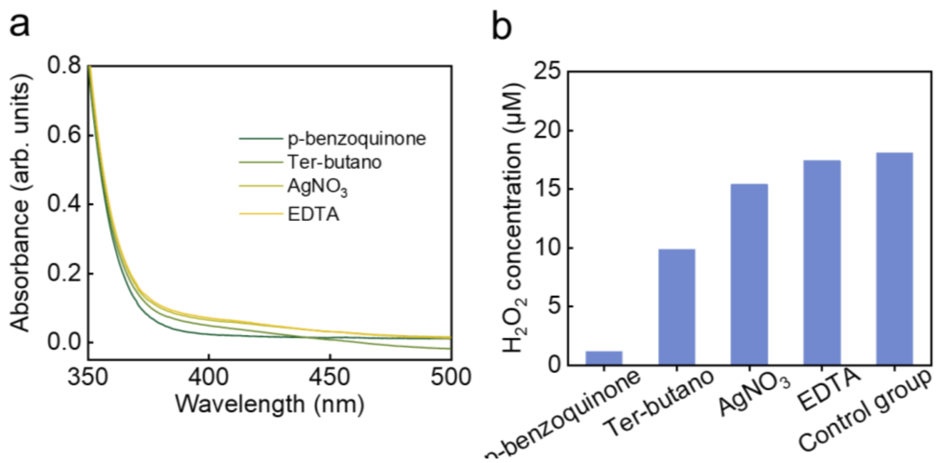

Figure S21 Effect of free radical scavengers on H_2O_2 production. a The absorption spectrum of an aqueous PTO solution with added free radical scavengers. **b** H_2O_2 production under different free radical scavengers.

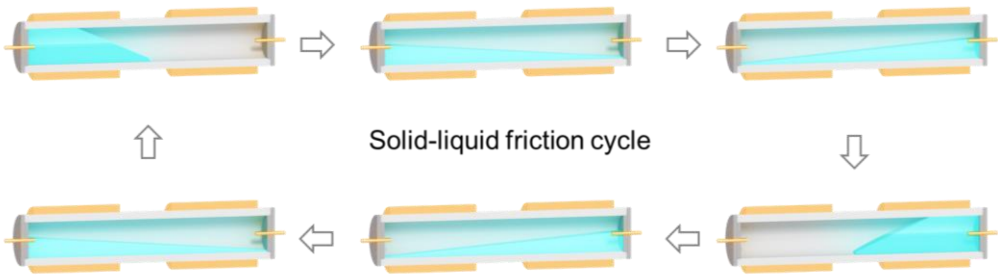

Figure S22 HEHG solid-liquid friction cycle

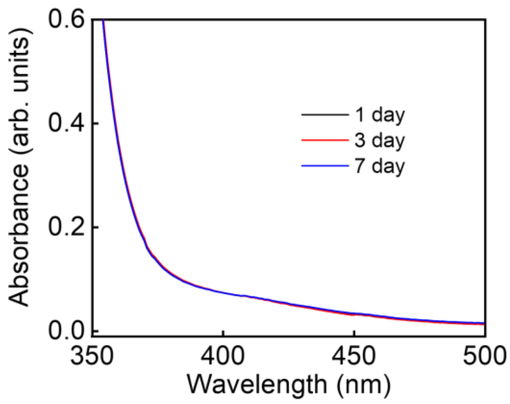

Figure S23 UV spectrum of PTO added to water after phase friction (the friction time was 1 day, 3 day and 7 day).

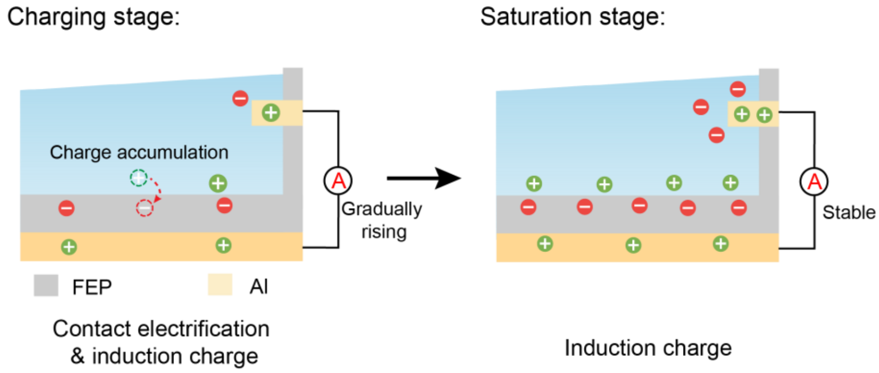

Figure S24 Solid-liquid power generation consists of the charging stage and the saturation stage.

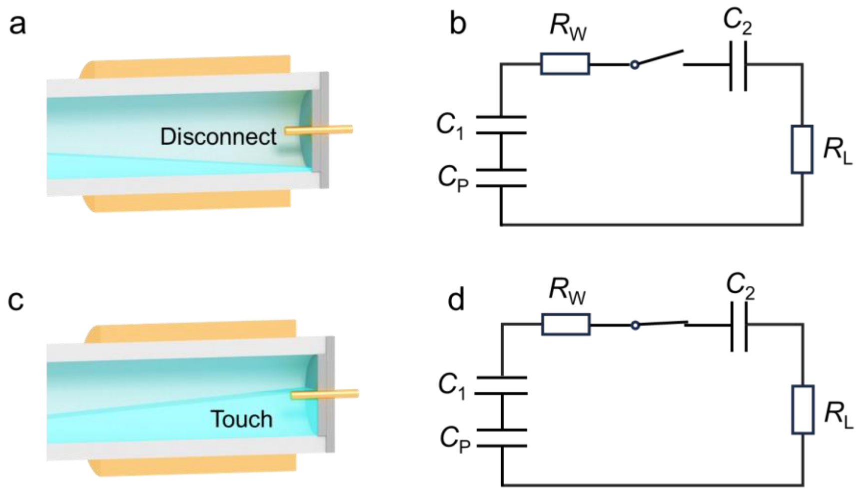

Figure S25 Circuit diagram of solid-liquid power generation. a, b When water in the tube does not contact the Ag electrode, the circuit is broken. **c, d** Upon water contact with the Ag electrode, the electrical signal is generated.

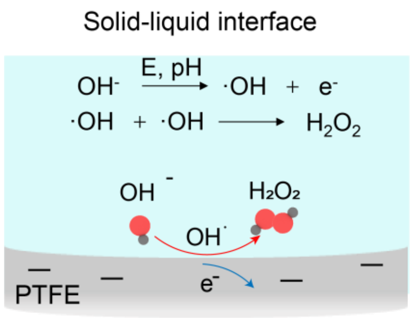

Figure S26 Interfacial electron transfer leads to the production of H_2O_2

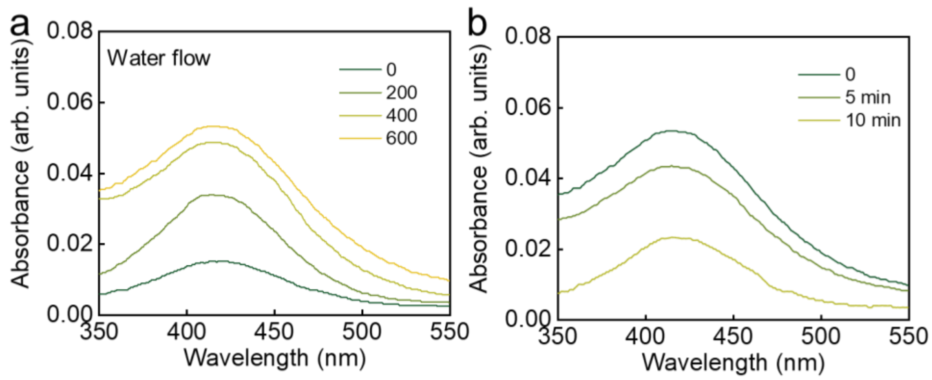

Figure S27 Characterization of OH concentration changes using O-phenylenediamine (OPD). a The friction cycle affects the concentration of ·OH produced. **b** UV absorption spectra at various time intervals after the friction cycle stopped. OPD can be oxidized by ·OH to generate diaminophenothiazine (DAP).

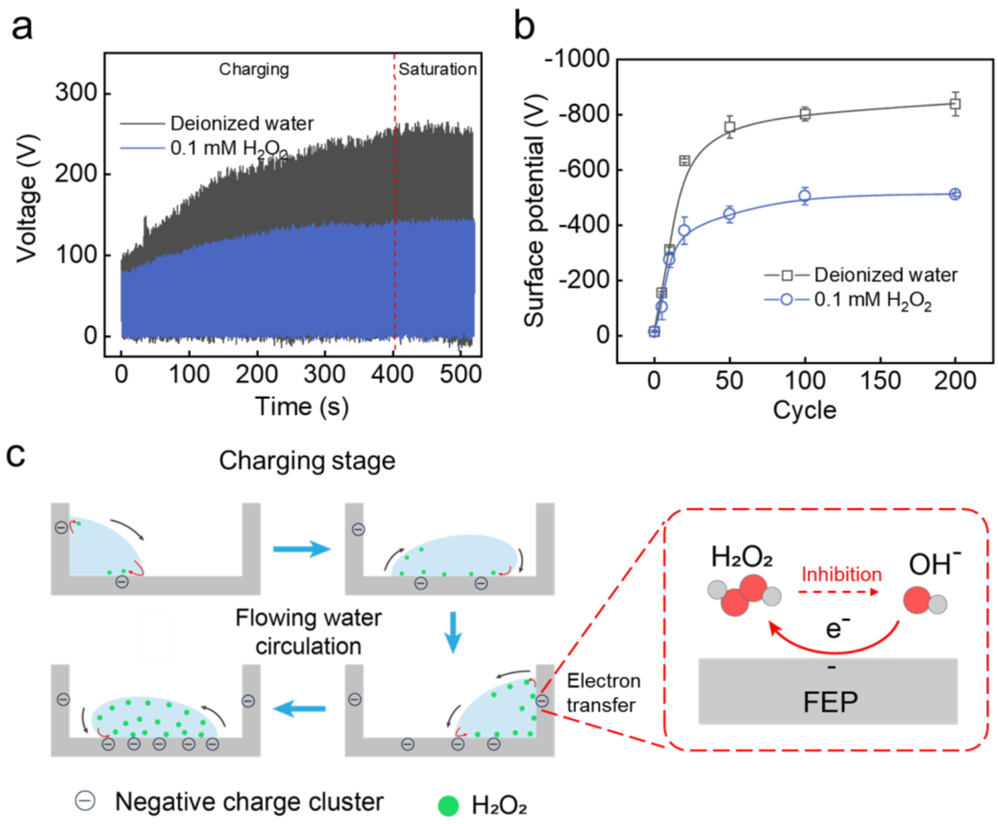

Figure S28 Effect of H_2O_2 on solid-liquid properties. a Effect of H_2O_2 on voltage performance of solid-liquid power generation (charging stage and saturation stage). **b** Effect of H_2O_2 on solid surface potential. **c** Electron transfer generates H_2O_2, and an excess amount of H_2O_2 has the potential to inhibit electron transfer. n = 3 independent samples for each group, data represent mean ± standard deviation.

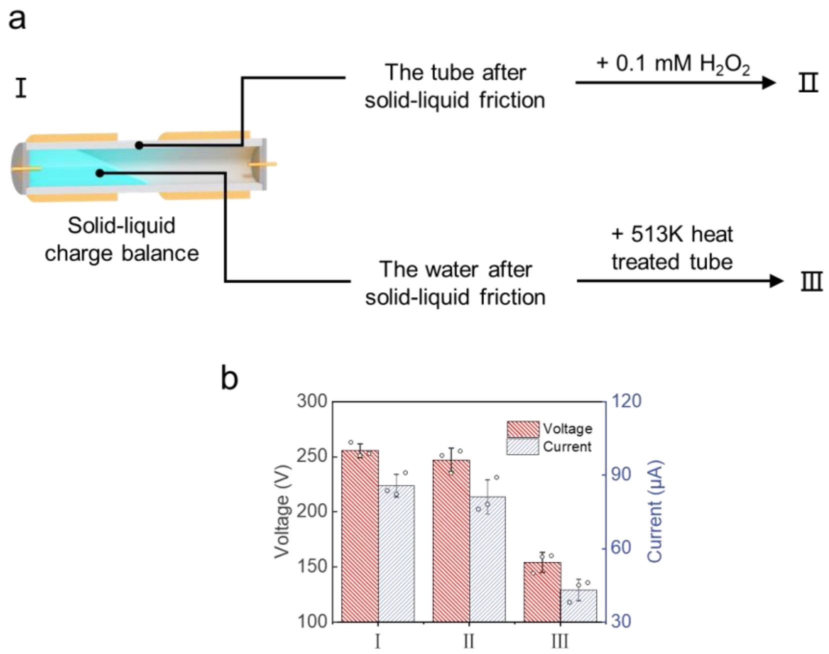

Figure S29 Effect of H_2O_2 on the solid-liquid electrical properties in the charging and saturation stages. a Experiment I Control group; Experiment II 0.1 mM H_2O_2 was added to the tube after solid-liquid friction; Experiment III Electron thermal excitation tube was added with water after solid-liquid friction. **b** Experiment I, II and III voltage and current performance. n = 4 independent samples for each group, data represent mean ± standard deviation.

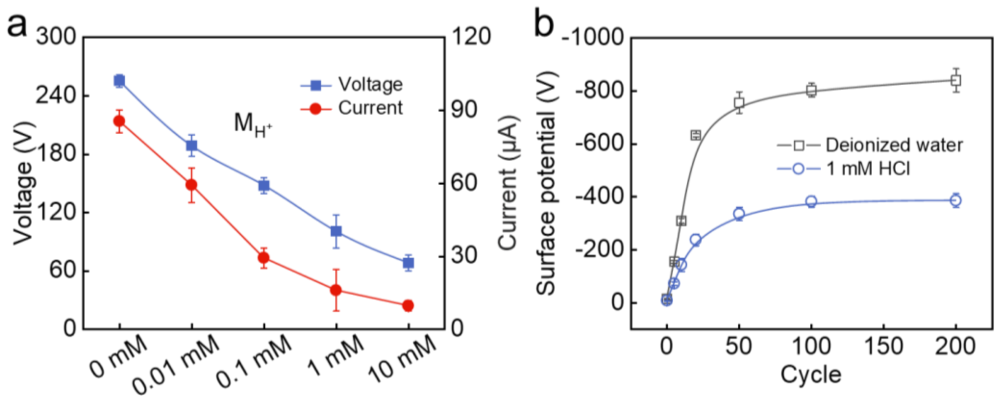

Figure S30 Effect of acid on solid-liquid electrical properties. a Effect of HCl concentration in liquid phase on electrical properties. **b** After solid-liquid friction, the solid surface potential. n = 3 independent samples for each group, data represent mean ± standard deviation.

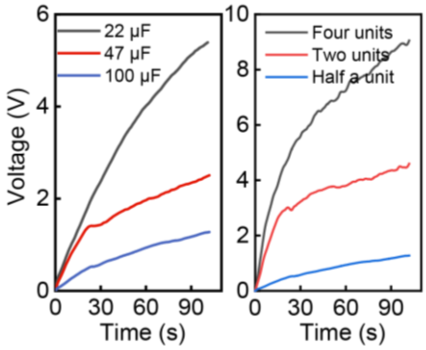

Figure S31 Charging performance of capacitors of different capacities with different numbers of power generation units.

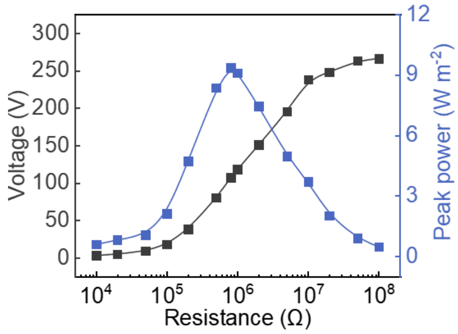

Figure S32 The output voltage when the external resistance changes from 1 Ω to 5×10^8 Ω, and the calculation of power output under different resistive loads.

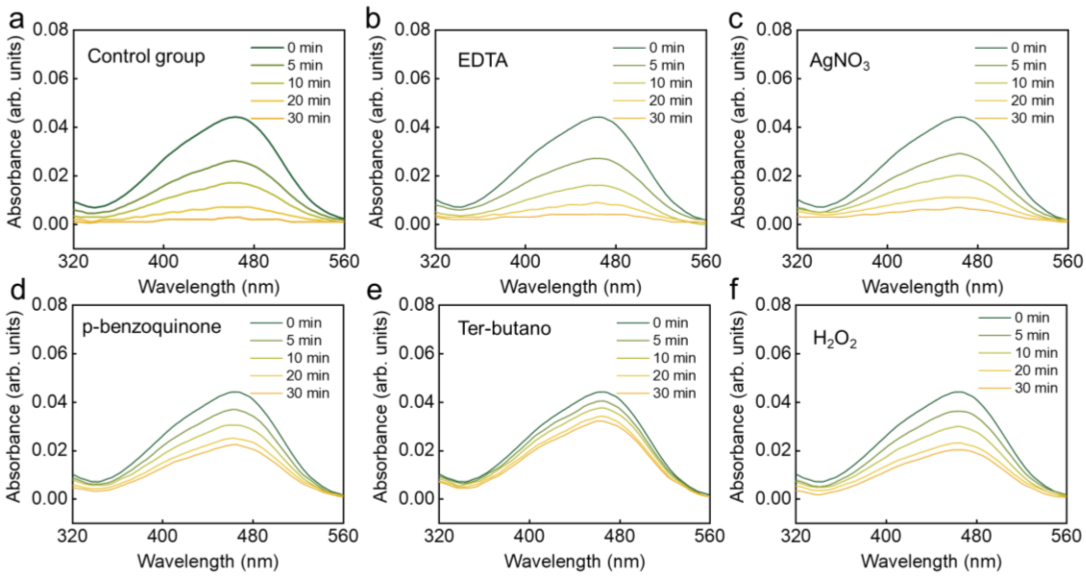

Figure S33 Effect of adding free radical scavengers or H_2O_2 to water on the degradation of methyl orange. a Control group. **b** 1 mM EDTA. **c** 1 mM $AgNO_3$. **d** 1 mM Ter-butano. **e** 1 mM p-benzoquinone. **f** 1 mM H_2O_2.

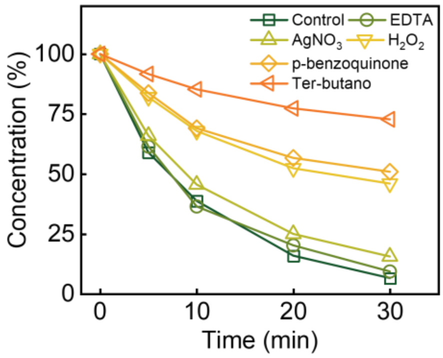

Figure S34 Changes in methyl orange concentration under free radical scavengers and H_2O_2.

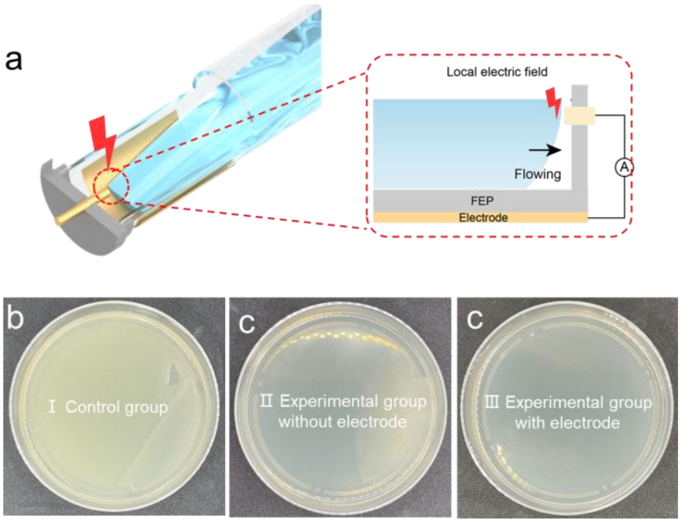

Figure S35 The antibacterial mechanism of the HEG device. a Local electric fields for antibacterial effects. **b, c, d** Plating photographs showing antibacterial experiment.

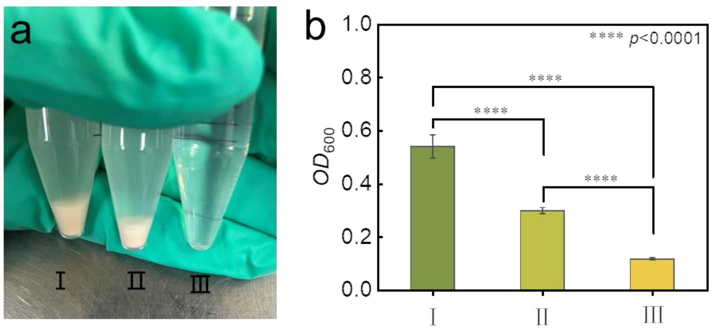

Figure S36 Antibacterial properties of HEG devices. n = 3 independent samples for each group, data represent mean ± standard deviation.

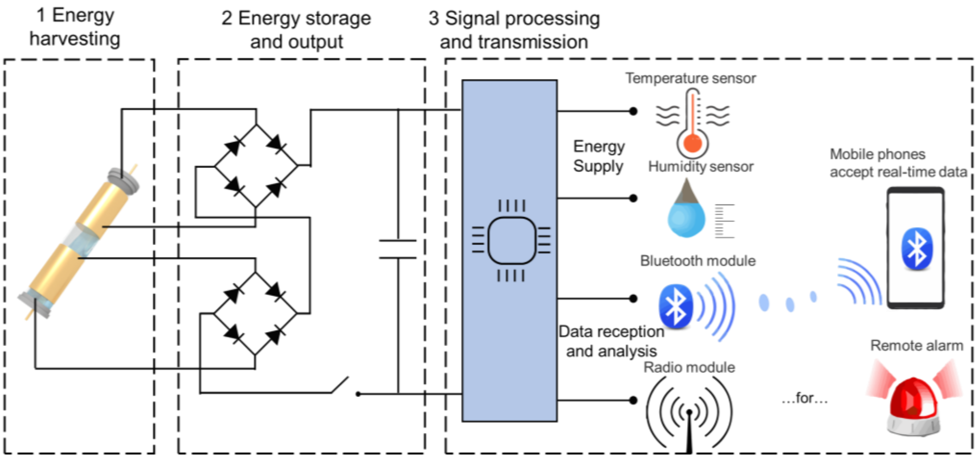

Figure S37 HEHG applied in maritime Internet of Things systems

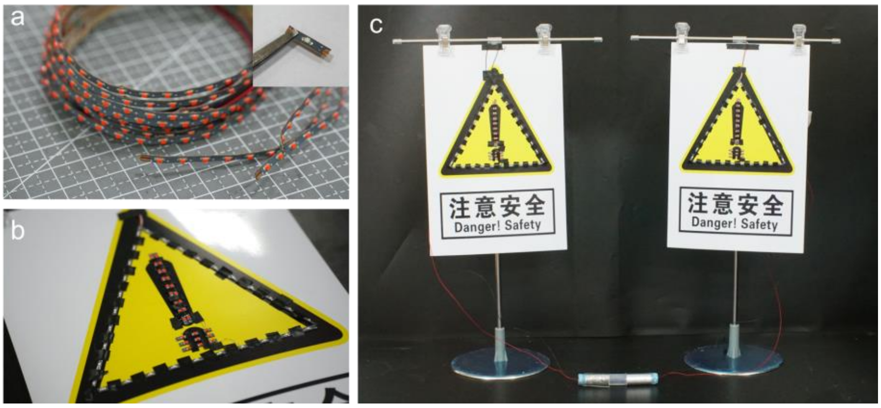

Figure S38 Preparation of warning light signs. a The light-emitting module is a light strip capable of emitting red and blue light. **b** Cut the light strips and connect them in series to the circuit. **c** A single HEHG unit can achieve the alternating lighting of two warning signs.

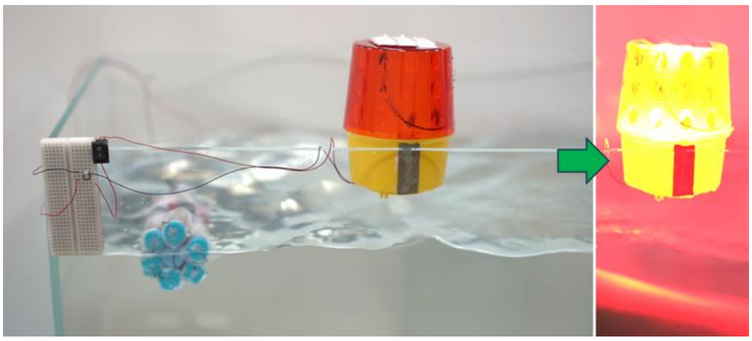

Figure S39 Seven integrated HEHGs can power a high-intensity lamp.

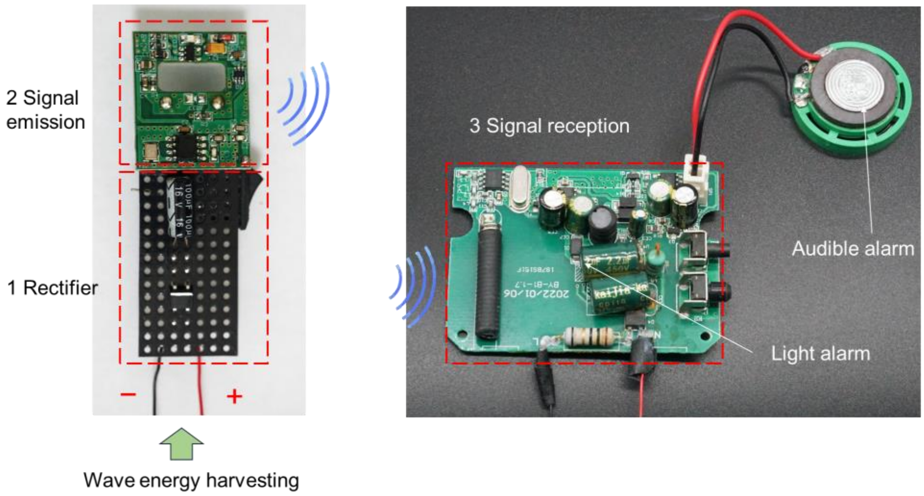

Figure S40 Wireless Monitoring System: The energy module, rectifier module, and information transmission module constitute an information transmission system. Upon receiving wireless information, the remote information receiving module emits two signals: light and sound.

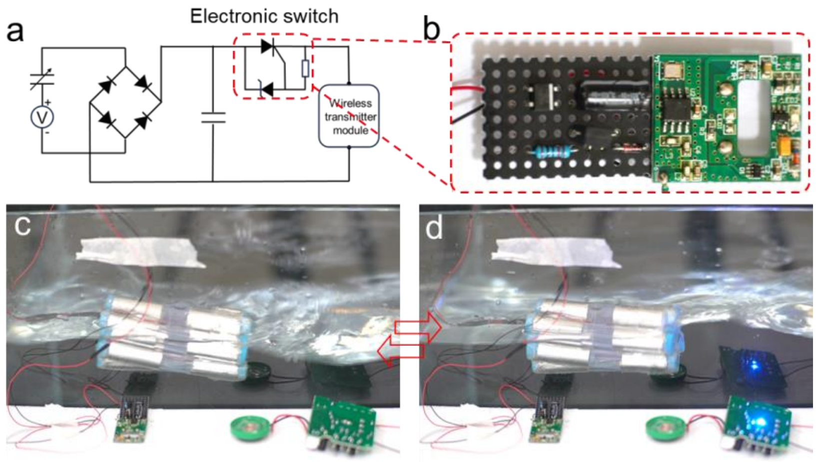

Figure S41 Wireless Monitoring System. **a** Electronic switch circuit diagram. **b** Electronic switch and wireless module device. c, d Wave-driven wireless signal transmission.

Table S1. Mechanism of spontaneous generation of H_2O_2.

Ref	System	H_2O_2 preparation method	H_2O_2 production mechanism
[1], [2]	Liquid/Gas	Spraying droplets	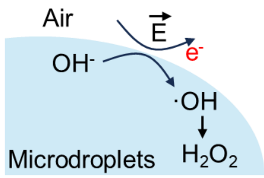
[3], [4]	Liquid/Solid	Particle/water ultrasound	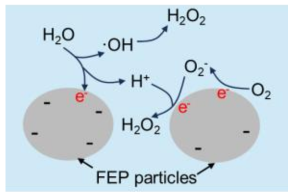
[5]	Liquid/Solid	Microfluidics injection	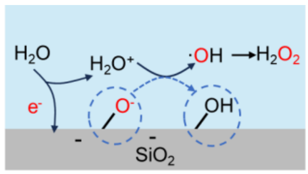
Our work	Liquid/Solid	Water flow	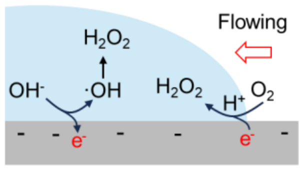

Table S2. Comparison of power output performance of HEG and related wave energy harvesting devices.

References	Type of device	Energy source (solid-liquid or solid-solid)	Peak Power Density (W/m^3)
[6]	TENG	S-L	0.228 W/m^3
[7]	TENG	S-S	0.91 W/m^3
[8]	TENG	S-S	6.67 W/m^3
[9]	TENG	S-L	13.1 W/m^3
[10]	TENG/EMG	S-S	18.98 W/m^3
[11]	TENG/EMG	S-S	31.6 W/m^3
[12]	TENG/EMG	S-S	162.01 W/m^3
[13]	TENG	S-S	200 W/m^3
[14]	TENG	S-S	358 W/m^3
Our work	TENG	S-L	Half ≈ 2877 W/m^3 Single ≈ 5754 W/m^3

1. Lee, J. K. et al. Spontaneous generation of hydrogen peroxide from aqueous microdroplets. *Proc. Natl. Acad. Sci.* **116**, 19294-19298 (2019).
2. Lee, J. K. et al. Condensing water vapor to droplets generates hydrogen peroxide. *Proc. Natl. Acad. Sci.* **117**, 30934-30941 (2020).
3. Berbille, A. et al. Mechanism for generating H_2O_2 at water-solid interface by contact-electrification. *Adv. Mater.* **35**, 2304387 (2023).
4. Zhao, J. et al. Contact-electro-catalysis for direct synthesis of H_2O_2 under ambient conditions. *Angew. Chem. Int. Ed. Engl.* **62**, 202300604 (2023).
5. Chen, B. et al. Water-solid contact electrification causes hydrogen peroxide production from hydroxyl radical recombination in sprayed microdroplets. *Proc.*

Natl. Acad. Sci. **119**, 2209056119 (2022).
6. Ouyang, R., Huang, Y., Ye, H., Zhang, Z. & Xue, H. Copper particles-PTFE tube based triboelectric nanogenerator for wave energy harvesting. *Nano Energy* **102**, 107749 (2022).
7. Zhang, Q. et al. High performance liquid-solid tubular triboelectric nanogenerator for scavenging water wave energy. *Nano Energy* **103**, 107810 (2022).
8. Jung, H., Ouro-Koura, H., Salalila, A., Salalila, M. & Deng, Z. D. Frequency-multiplied cylindrical triboelectric nanogenerator for harvesting low frequency wave energy to power ocean observation system. *Nano Energy* **99**, 107365 (2022).
9. Wu, H., Wang, Z. & Zi, Y. Multi-mode water-tube-based triboelectric nanogenerator designed for low-frequency energy harvesting with ultrahigh volumetric charge density. *Adv. Energy Mater.* **11**, 2100038 (2021).
10. Han, C. et al. Hybrid triboelectric-electromagnetic nanogenerator with a double-sided fluff and double halbach array for wave energy harvesting. *Adv. Funct. Mater.* **32**, 2205011 (2022).
11. Hong, H. et al. Self-powered seesaw structured spherical buoys based on a hybrid triboelectric–electromagnetic nanogenerator for sea surface wireless positioning. *Energ. Environ. Sci.* **15**, 621-632 (2022).
12. Zhu, C. et al. Highly integrated triboelectric-electromagnetic wave energy harvester toward self-powered marine buoy. *Adv. Energy Mater.* **13**, 2301665 (2023).
13. Zhang, C. et al. Bifilar-pendulum-assisted multilayer-structured triboelectric nanogenerators for wave energy harvesting. *Adv. Energy Mater.* **11**, 2003616 (2021).
14. Zhang, C. et al. High space efficiency hybrid nanogenerators for effective water wave energy harvesting. *Adv. Funct. Mater.* **32**, 2111775 (2022).